

OPTICS

Ideal Weyl points and helicoid surface states in artificial photonic crystal structures

Biao Yang,^{1*} Qinghua Guo,^{1,2*} Ben Tremain,^{3*} Rongjuan Liu,^{4*} Lauren E. Barr,³ Qinghui Yan,⁴ Wenlong Gao,¹ Hongchao Liu,¹ Yuanjiang Xiang,² Jing Chen,⁵ Chen Fang,⁴ Alastair Hibbins,^{3,†} Ling Lu,^{4,†} Shuang Zhang^{1,†}

Weyl points are the crossings of linearly dispersing energy bands of three-dimensional crystals, providing the opportunity to explore a variety of intriguing phenomena such as topologically protected surface states and chiral anomalies. However, the lack of an ideal Weyl system in which the Weyl points all exist at the same energy and are separated from any other bands poses a serious limitation to the further development of Weyl physics and potential applications. By experimentally characterizing a microwave photonic crystal of saddle-shaped metallic coils, we observed ideal Weyl points that are related to each other through symmetry operations. Topological surface states exhibiting helicoidal structure have also been demonstrated. Our system provides a photonic platform for exploring ideal Weyl systems and developing possible topological devices.

Topology is the mathematics of conserved properties under continuous deformations, and the recent study of band topologies is yielding a suite of fascinating interface transport phenomena that include one-way propagation of energy and previously unknown relativistic behavior. The two-dimensional honeycomb lattice is the most studied in the exploration of topological phenomena. Made famous by graphene (1), the energy-momentum dispersion in a honeycomb system is linear, and the crossings of bands in energy-momentum space are known as Dirac points. The transport of the

quasiparticles around these points is massless, and this remarkable transport behavior is associated with the “hidden” symmetry associated with its two identical sublattices. Weyl points are the characteristic of an analogous phenomenon when the lattice is extended to three dimensions (2–5). In electronic systems, materials exhibiting Weyl points are known as Weyl semimetals, and Weyl fermion is the solution to the massless Dirac equation. Each Weyl point can be assigned an integer “charge” based on its chirality, known as the Chern number, and much like magnetic monopoles, Weyl points are only ever found in pairs of

opposite charge. Just like Dirac points, these Weyl points also exist in photonic systems, but unlike Dirac points, they can only exist once either (or both) time-reversal or space-inversion symmetry of the crystal is broken. To date, Weyl points of various forms have been proposed and realized in several boson or fermion systems (2–4, 6–13). Among them, the presence of surface state arcs as one of the fingerprints of Weyl systems has been observed.

However, demonstration of more fundamental topological features of Weyl points—such as the helicoidal dispersion, which yields the open Fermi arcs of topological surface states (14)—has been hindered by the complicated configuration of energy bands at the Weyl energy. Moreover, some realistic and innovative device applications critically depend on a simple embodiment of Weyl systems (5). Thus, an ideal Weyl system (15–17) has attracted much attention because in such systems, all Weyl nodes are symmetry-related, residing at the same energy with a large momentum separation and devoid of nontopological bands in a sufficiently large energy interval.

Although Weyl degeneracies can be readily found by breaking either time-reversal or

¹School of Physics and Astronomy, University of Birmingham, Birmingham B15 2TT, UK. ²International Collaborative Laboratory of 2D Materials for Optoelectronic Science and Technology of Ministry of Education, Shenzhen University, Shenzhen 518060, China. ³Electromagnetic and Acoustic Materials Group, Department of Physics and Astronomy, University of Exeter, Stocker Road, Exeter EX4 4QL, UK. ⁴Institute of Physics, Chinese Academy of Sciences/Beijing National Laboratory for Condensed Matter Physics, Beijing 100190, China. ⁵School of Physics, Nankai University, Tianjin 300071, China.

*These authors contributed equally to this work.

†Corresponding author. Email: a.p.hibbins@exeter.ac.uk (A.H.); linglu@iphy.ac.cn (L.L.); s.zhang@bham.ac.uk (S.Z.)

Fig. 1. Structure and band topology of the ideal photonic Weyl meta-crystal.

(A) Schematic of a saddle-shaped metallic inclusion, which has non-centrosymmetric D_{2d} point group symmetry, embedded in a dielectric (dielectric constant of $2.2 \pm 2\%$ at 10 GHz). Here, period $a_x = a_y = a = 3$ mm and $a_z = 4.5$ mm. (B) Photograph of the top surface of the sample, fabricated with printed circuit board technology by etching 3-mm-thick, double-sided, copper-clad (0.035 mm-thick) dielectric laminates. A 1.5-mm-thick “blank” layer spaces each pair of printed layers so as to prevent electrical connection between the metallic coils. The bulk sample is assembled by stacking (1.5 + 3)-mm bilayers in the z direction. The unit cell is indicated by the white square. (C) Four type-I Weyl points reside on the same energy, as indicated by the blue plane with respect to $k_z = 0$. (D) Bulk and surface BZ with four Weyl points located along the Γ –M directions. Top (magenta) and bottom (cyan) topological surface-state arcs are shown schematically. (E) CST Microwave Studio (CST) simulated band structure along high-symmetry lines. The blue shaded area highlights the energy window where the ideal Weyl points (red and blue points) reside. Longitudinal mode (LM) and transverse mode (TM) are labeled.

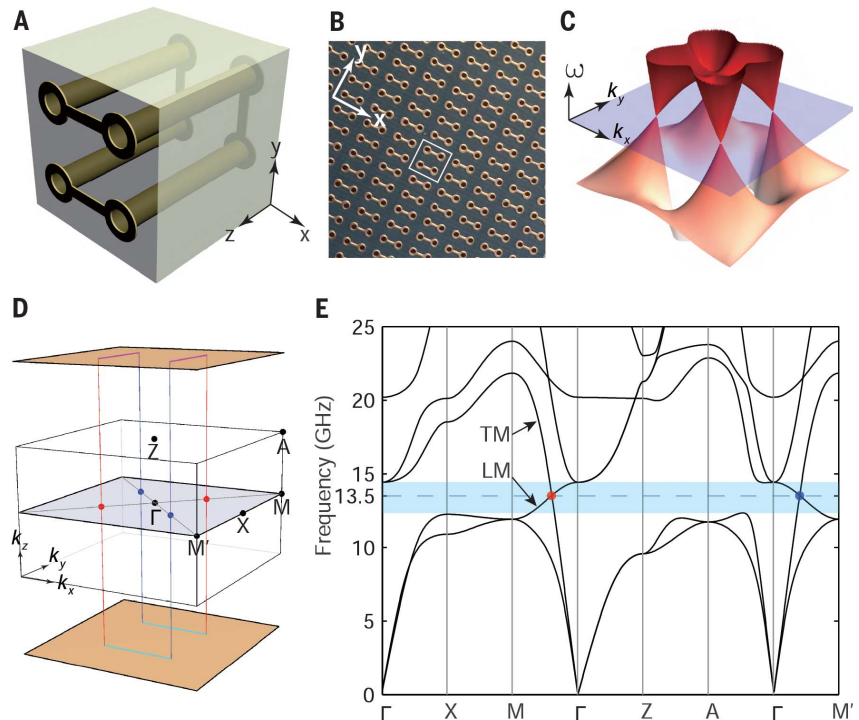
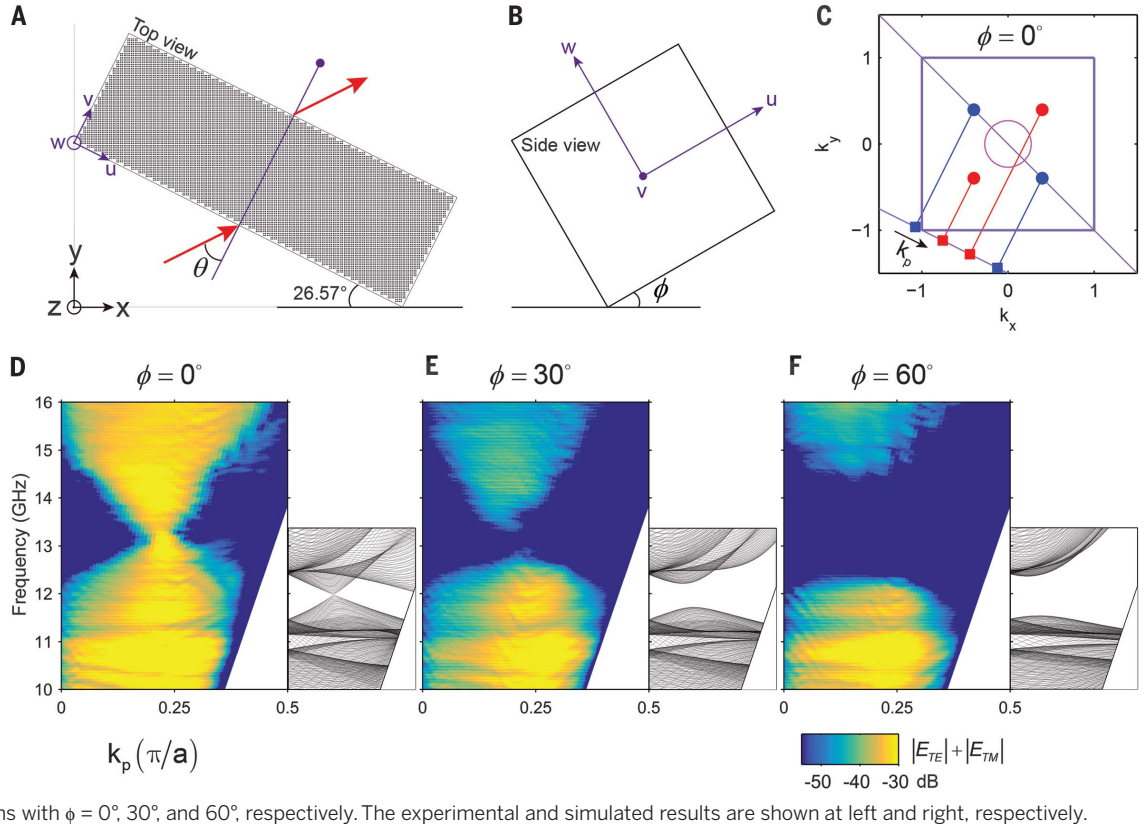


Fig. 2. Angle-resolved transmission measurement of the ideal Weyl system. (A and B) Schematic view of the sample fabricated with crystal cutting angle of 26.57° . Top and side views are illustrated. θ and ϕ are the rotation angles defined around the z and v axes, respectively. (C) Projection of Weyl points in momentum space with respect to the global coordinates (x, y, z) when $\phi = 0^\circ$. First BZ is indicated by the purple square. Magenta circle indicates the equifrequency contour of vacuum at 13.5 GHz. k_p is the in-plane component of the incident wave vector through a projection onto the sample surface (u - w surface) (9). (D, E, and F) The band projections with $\phi = 0^\circ, 30^\circ,$ and 60° , respectively. The experimental and simulated results are shown at left and right, respectively.



inversion symmetry (5), or both, the experimental realization of a truly ideal Weyl system has not yet been reported. Here, we explore the microwave response of a three-dimensional photonic crystal composed of metallic inclusions (termed a “meta-crystal”) in order to realize an ideal Weyl system protected by D_{2d} point symmetry. Our meta-crystal exhibits four Weyl points at the same energy, the minimum number allowed in the presence of time-reversal symmetry. By placing an excitation point-source on one surface of the crystal, and scanning the near fields on the opposite surface, we observed the intriguing helicoidal structure of topological surface states: a physical representation of Riemann surface generated by a multivalued function (14).

Our meta-crystal design offers an ideal platform for the investigation of various unconventional physics in Weyl systems. The symmetry of the studied meta-crystal belongs to the simple tetragonal lattice with symmorphic space group $P4m2$ (no. 115). The basis comprises a saddle-shaped connective metallic coil (Fig. 1, A and B) that possesses D_{2d} (4_2m in Hermann-Mauguin notation) point group symmetry. The system has no spatial inversion. These metallic elements support localized electromagnetic resonances with current distributions that can be expanded into multipolar modes (18). In an effective medium model (supplementary materials section 4 and fig. S1) (19), these resonances collectively exhibit a bi-anisotropic effect, leading to a directionally dependent chirality response (20). Here, the unavoidable crossings between the longitudinal

mode (LM) with negative dispersion and the transverse electric mode (TM) with positive dispersion along Γ -M result in the formation of a type-I Weyl point (Fig. 1C and fig. S2) (19, 21). Analysis via the irreducible representation of the point group shows that these two modes belong to two different classes, with eigenvalues ± 1 of C_2 rotation along Γ -M (Fig. 1D), where level repulsion is forbidden (supplementary materials section 5 and fig. S3) (19). The other three Weyl points are obtained after application of the D_{2d} symmetry operation. For instance, three twofold rotation symmetries (C_2 and $2C_2'$) combined with time-reversal symmetry guarantee that these four Weyl nodes are located on the Γ -M at the same frequency, at which application of two mirror symmetries (σ_x and σ_y) reverses the corresponding topological charges. The simulated band structure along high-symmetry lines is shown in Fig. 1E (as defined in Fig. 1D) in the Brillouin zone (BZ), where a pair of Weyl points resides at the same frequency. As such, these Weyl degeneracies appear in a relatively large energy window (~ 2.1 GHz around the frequency of the Weyl point) (Fig. 1E, blue shaded region) that is also devoid of other bulk bands and hence unequivocally facilitates their experimental identification.

The linear band crossings of the bulk states around the Weyl point are confirmed with angle-resolved transmission measurements (9). In order to couple energy across the meta-crystal, the momentum of the bulk states must be matched to the in-plane momentum of an incident wave; a sample with special crystal cutting is fabri-

cated (Fig. 2A), in which the crystal orientation forms an angle of 26.57° with one of the cutting boundaries. Compared with the global axis, xyz , a local coordinate, uvw , is defined. The length (along u), width (along v), and height (along w) of the sample are 300, 100, and 300 mm, respectively. Two angles, θ and ϕ (Fig. 2, A and B), are scanned to obtain the angle-resolved transmission spectrum. With this specific crystal cutting, when $\phi = 0^\circ$, Weyl points in BZ are projected along the scan wave vector k_p , which is related to θ , as indicated in Fig. 2C. Obviously, two of the projected Weyl points are located within the light circle (magenta circle) at the Weyl frequency (13.5 GHz). Thus, even a plane wave illuminated directly from air onto the sample can address these two Weyl points. Comparisons between the simulation and experiment results are shown in Fig. 2, D, E, and F. In Fig. 2D, with $\phi = 0^\circ$, a linear gapless energy dispersion is obtained, and the density of states vanishes at the Weyl frequency because of the absence of other bulk states at the same frequency in an ideal Weyl system. After rotating the sample to $\phi = 30^\circ$ and 60° around the v axis, a complete gap is observed as expected.

Another direct manifestation of the topological aspects of a Weyl system is the exotic topological surface states taking the form of arcs connecting the topologically distinct bulk states. Following a closed contour around an end of the arcs, one moves between the lower (valence) and upper (conduction) bands (14), which is a direct consequence of the chiral characteristic of Weyl

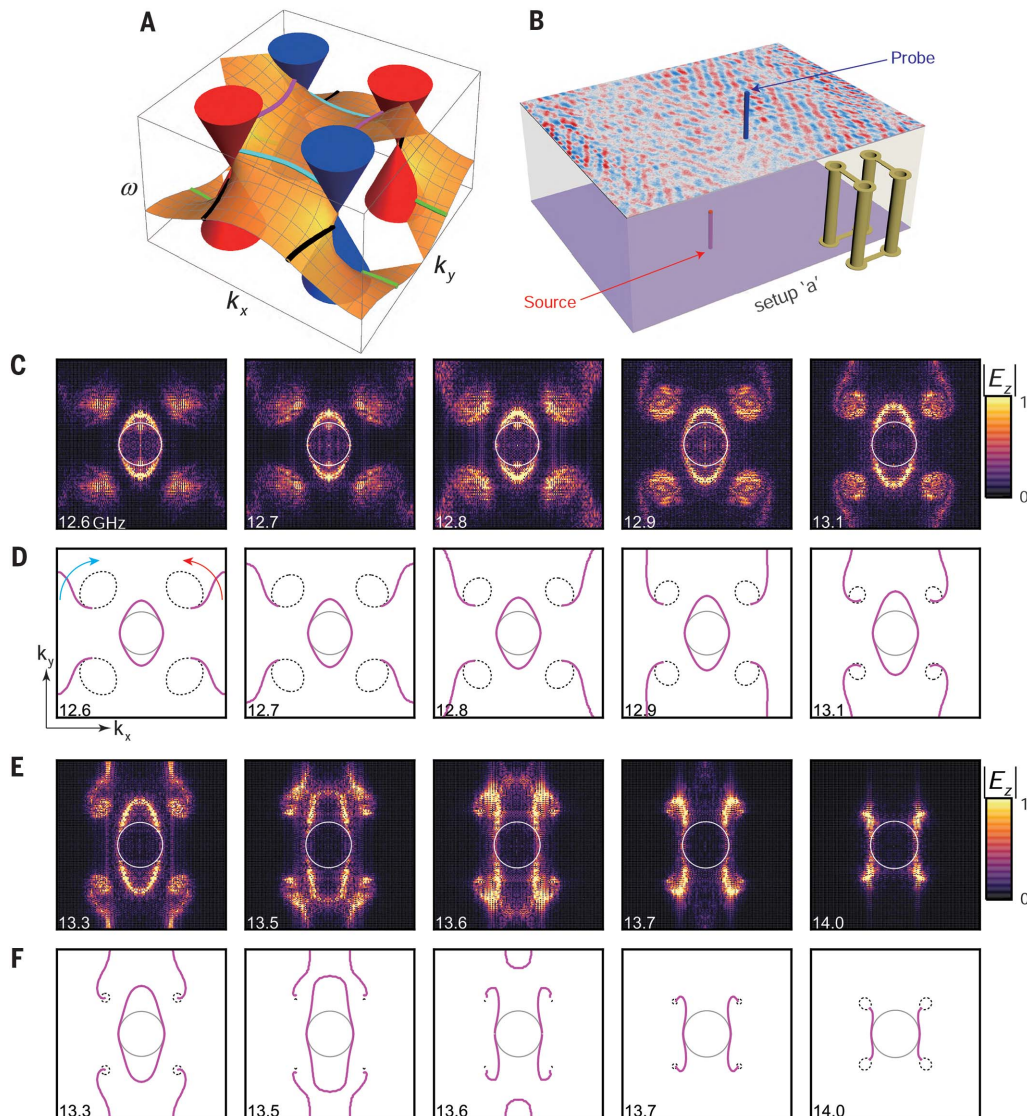


Fig. 3. Experimental observation of helicoidal structure of topological surface states.

(A) Schematic illustration of helicoid surface states in an ideal Weyl system, with four Weyl points within the surface BZ, plotted by using the Jacobi elliptic function. The arcs of different colors represent the evolution of equifrequency arcs connecting Weyl points of opposite Chern numbers. (B) Transmitted near-field scanning system (setup “a”), where the source (red) is positioned on the bottom surface center. (C and E) Equifrequency contour ($|E_z|$) measured by using setup “a” from 12.6 to 14.0 GHz. (D and F) Bulk (black dashed) and surface (magenta solid) states simulated with, correspondingly. Anticlockwise (red) and clockwise (cyan) arrows indicate the surface arc rotation directions with increasing frequency corresponding to positive and negative Weyl nodes, respectively. The central solid circle indicates the air equifrequency contour. The plotted range for each panel is $[-\pi/a, \pi/a]^2$.

nodes, as schematically shown in Fig. 3A. It is well known that the gapless surface states of Weyl crystals take the form of helicoid Riemann surfaces (14), where the bulk Weyl points correspond to the poles and zeros adopting the sign of their respective Chern numbers. Recently, it was shown that topological surface states of double Weyl systems can be analytically expressed, across the entire BZ, as the double-periodic Weierstrass elliptic function (22). Because the Weierstrass elliptic function has one second-order pole and one second-order zero, it is not the most fundamental expression of the Weyl surface states. Here, we show that our ideal-Weyl meta-crystal of four Weyl points has surface states whose dispersion is topologically equivalent to the argument of Jacobi elliptic function $\text{cn}(z, m)$ of two poles and two zeros on the complex plane. $\text{cn}(z, m)$ is a meromorphic function with periods $4K(m)$ and $4K(1 - m)$, where K is the complete elliptic integrals of the first kind. For our system, the mapping is given by $\omega(k_x, k_y) \sim \arg\{\text{cn}[(k_x - k_y)/2 + (k_x + k_y)i/2, 1/2]\}$, as plotted in Fig. 3A.

The helicoidal structure of the surface arcs was probed by using the transmitted near-field scanning configuration, with the excitation source located at the center of the bottom layer of the meta-crystal stack (Fig. 3B, setup “a”), where the detecting probe can raster-scan the top surface so as to map out both the bulk and surface modes. Another configuration (fig. S4B, setup “b”), in which the excitation source is positioned at the edge or corner of the top surface, is also used to identify the surface states. These two setups provide complementary information for the observation of helicoid surface states. In all near-field measurements, we set the scanning step as 1 mm ($a/3$), providing a large surface momentum space in the range of $(-3\pi/a, 3\pi/a)^2$ after the Fourier transformation. The helicoid structure of the surface arc was experimentally measured and numerically simulated and is presented as a series of equifrequency contours between 12.6 and 14.0 GHz (Fig. 3, C and E, in experiment, and Fig. 3, D and F, in simulation).

As shown in Fig. 3, C and D, at 13.1 GHz, which is below the Weyl frequency, the Fourier transformation of the experimentally measured field distribution shows the presence of four symmetrically displaced elliptical bulk states with the same size located along the diagonal directions. We clearly observed two surface arcs running across the BZ boundaries and connecting the neighboring bulk states with opposite topological charges. In the vicinity of the air equifrequency contour (circle), there exists a surface ellipse. The surface ellipse joins and reroutes the surface arc at higher frequencies (Fig. 3, E and F). Indeed, the surface ellipse and surface arcs together form the same unified helicoid surface in the dispersion of the surface states.

With increasing frequency, the top surface arc that emerged from the Weyl node with positive and negative topological charge rotates anticlockwise and clockwise, respectively. The observed rotation of the helicoid surface state around a Weyl node can therefore be used to detect the chirality of the Weyl node (23). As mentioned above, at

lower frequencies each surface arc connects between the bulk states through the BZ boundary, whereas the surface ellipse expands gradually with increasing frequency. Between 13.5 and 13.6 GHz, the surface arc and surface ellipse connect with each other and then transition into a new configuration: a direct surface arc connecting between the bulk states within the BZ, and a surface ellipse centered at its edge. The evolution of the surface arc configuration across the measured frequency range matches topologically with that described by the Jacobi elliptic function shown in Fig. 3A. At the frequency of 14.3 GHz, the surface arcs appear to be linear (fig. S4F) (19), leading to nearly diffractionless propagation of the surface wave in the real space (fig. S4C) (19). Slightly away from the Weyl frequency, the equi-energy contour of the bulk state consists of four very small spheres enclosing the Weyl points. It is expected that the interference between them results in a chessboard-like interference pattern in real space, which is experimentally confirmed as a spatial frequency filter (fig. S5) (17, 19). In addition, the dimensional reduction from ideal Weyl points to graphene-like dispersion is shown in fig. S6 (supplementary materials section 8) (19). We also analyzed that the presence of dielectric loss of our system does not affect the existence of the Weyl points (supplementary materials section 9) (19).

The designed ideal Weyl system presented here opens up opportunities for studying intriguing physics and offers a prototype platform for realistic device applications. In photonics, besides the topologically nontrivial surface states sup-

ported by Weyl materials, the diverging Berry curvature (5) close to Weyl points provides a new degree of freedom in controlling the transport of optical wave packets and may lead to the observation of a gigantic Hall effect for light (24). Furthermore, any phenomena related to the conical dispersion of the light cone may be observed around Weyl points, such as diverging and diminishing scattering cross sections (25). The vanishing density of states at Weyl frequencies also provides a robust platform for controlling light-matter interaction when emitters are embedded inside photonic Weyl materials.

REFERENCES AND NOTES

1. A. H. Castro Neto, F. Guinea, N. M. R. Peres, K. S. Novoselov, A. K. Geim, *Rev. Mod. Phys.* **81**, 109–162 (2009).
2. X. Wan, A. M. Turner, A. Vishwanath, S. Y. Savrasov, *Phys. Rev. B* **83**, 205101 (2011).
3. A. A. Burkov, L. Balents, *Phys. Rev. Lett.* **107**, 127205 (2011).
4. G. Xu, H. Weng, Z. Wang, X. Dai, Z. Fang, *Phys. Rev. Lett.* **107**, 186806 (2011).
5. N. P. Armitage, E. J. Mele, A. Vishwanath, arXiv:1705.01111 [cond-mat.str-el] (2017).
6. S.-Y. Xu et al., *Science* **349**, 613–617 (2015).
7. H. Weng, C. Fang, Z. Fang, B. A. Bernevig, X. Dai, *Phys. Rev. X* **5**, 011029 (2015).
8. A. A. Soluyanov et al., *Nature* **527**, 495–498 (2015).
9. L. Lu et al., *Science* **349**, 622–624 (2015).
10. L. Huang et al., *Nat. Mater.* **15**, 1155–1160 (2016).
11. W.-J. Chen, M. Xiao, C. T. Chan, *Nat. Commun.* **7**, 13038 (2016).
12. J. Noh et al., *Nat. Phys.* **13**, 611–617 (2017).
13. B. Yang et al., *Nat. Commun.* **8**, 97 (2017).
14. C. Fang, L. Lu, J. Liu, L. Fu, *Nat. Phys.* **12**, 936–941 (2016).
15. J. Ruan et al., *Nat. Commun.* **7**, 11136 (2016).
16. J. Ruan et al., *Phys. Rev. Lett.* **116**, 226801 (2016).
17. L. Wang, S.-K. Jian, H. Yao, *Phys. Rev. A* **93**, 061801 (2016).
18. T. Kaelberer, V. A. Fedotov, N. Papasimakis, D. P. Tsai, N. I. Zheludev, *Science* **330**, 1510–1512 (2010).
19. Materials and methods are available as supplementary materials.
20. Q. Guo, W. Gao, J. Chen, Y. Liu, S. Zhang, *Phys. Rev. Lett.* **115**, 067402 (2015).
21. M. Xiao, Q. Lin, S. Fan, *Phys. Rev. Lett.* **117**, 057401 (2016).
22. T. Zhang et al., arXiv:1705.07244 [cond-mat.mtrl-sci] (2017).
23. Q. Ma et al., *Nat. Phys.* **13**, 842–847 (2017).
24. M. Onoda, S. Murakami, N. Nagaosa, *Phys. Rev. Lett.* **93**, 083901 (2004).
25. M. Zhou et al., *Nat. Commun.* **8**, 1388 (2017).

ACKNOWLEDGMENTS

This work was financially supported by the European Research Council Consolidator Grant (Topological), Horizon 2020 Action Project grant 734578 (D-SPA), and Leverhulme Trust (grant RPG-2012-674). S.Z. acknowledges support from the Royal Society and Wolfson Foundation. B.Y. acknowledges support from China Scholarship Council (grant 201306110041). Q.G. acknowledges the financial support of the National Natural Science Foundation of China (grant 11604216). Y.X. acknowledges support from the National Natural Science Foundation of China (grant 61490713). L.E.B. and A.H. acknowledge financial support from the Engineering and Physical Sciences Research Council of the United Kingdom (grant EP/L015331/1). C.F. was supported by the National Key Research and Development Program of China under grant 2016YFA0302400 and by the National Natural Science Foundation of China (NSFC) under grant 11674370. L.L. was supported by the National Key R&D Program of China under grants 2017YFA0303800 and 2016YFA0302400 and by NSFC under project 11721404. Near-field scanning data were collected by a vector network analyzer controlled with xyz-stage at G31 at the Department of Physics and Astronomy, University of Exeter, UK. All data created during this research are openly available from the University of Exeter's institutional repository at <http://hdl.handle.net/10871/30744>.

SUPPLEMENTARY MATERIALS

www.sciencemag.org/content/359/6379/1013/suppl/DC1
Materials and Methods
Supplementary Text
Figs. S1 to S6
References (26, 27)

4 October 2017; accepted 19 December 2017
Published online 11 January 2018
10.1126/science.aag1221



Supplementary Material for

Ideal Weyl points and helicoid surface states in artificial photonic crystal structures

Biao Yang, Qinghua Guo, Ben Tremain, Rongjuan Liu, Lauren E. Barr, Qinghui Yan, Wenlong Gao, Hongchao Liu, Yuanjiang Xiang, Jing Chen, Chen Fang, Alastair Hibbins,* Ling Lu,* Shuang Zhang*

*Corresponding author. Email: a.p.hibbins@exeter.ac.uk (A.H.); linglu@iphy.ac.cn (L.L.); s.zhang@bham.ac.uk (S.Z.)

Published 11 January 2018 as *Science* First Release
DOI: 10.1126/science.aaq1221

This PDF file includes:

Materials and Methods
Supplementary Text
Figs. S1 to S6
References

Materials and Methods

1. Sample fabrication

The sample was fabricated by a commercial company named *Shenzhen Sunsoar Circuit Technology* (<http://www.oem-pcb.com>) in Shenzhen, China, following the traditional Printed Circuit Board (PCB) fabrication technology. The technological details include: F4BM220 Material, board thickness 3.0mm, copper weight 1oz, no solder mask and surface leading OSP (Organic Solder-anility Preservative).

2. Near-field scanning setup and Fourier transformation

The experimental setup is schematically shown in Fig. 3B, we employ a microwave vector network analyzer (VNA) and a near-field antenna acting as a source (stationary) to provide excitation of electromagnetic surface waves, which are subsequently probed with a second near-field antenna (controlled by an xyz translation stage). The band structure of the surface states can then be determined from the Fourier analysis of the spatial distribution of the electric field at each frequency. In the scanning measurements, the scan step is set to be 1 mm, which is 1/3 of the lattice constant of the surface primitive unit cell ($3 \times 3 \text{ mm}^2$). Consequently, the maximum surface k-space has a range of $[-3\pi/a, 3\pi/a]^2$ after Fourier transformation.

3. Source and probe antennas

The measurement is performed in the microwave regime using a VNA to sweep the frequency (8–18 GHz), with a near-field antenna connected to the excitation/detection port. The antenna consists of a coaxial cable with a length (1 mm) of outer conductor and

sheath stripped away, leaving the central conductor (with core diameter 1 mm) exposed, which can provide efficient coupling to large-momentum bulk and surface modes benefitting from the broad range of momenta present in the exponentially decaying near field. The antenna also provides a method for measuring both the amplitude and the phase of the near field of the modes with sub-wavelength resolution. The probe is most sensitive to field components parallel to its orientation.

Supplementary Text

4. Modelled effective Hamiltonian and effective media analysis

The realistic photonic ideal Weyl semimetal consists of periodically buried saddle metallic coils in the substrate materials with dielectric constant of 2.2. Further analysis on the electromagnetic response reveals that the unit cell of saddle metallic coil can be viewed as two splitting resonance rings (SRR), which behave like two particles on each lattice, as schematically shown in Fig. S1.

By considering the motion of electrons driven by external electromagnetic field on those metallic components (27), we obtain,

$$\begin{aligned} red : -i\omega I + \omega_0^2 q &= \frac{1}{L} (E_y l + Ai\omega H_x) \\ blue : -i\omega I + \omega_0^2 q &= \frac{1}{L} (E_x l + Ai\omega H_y) \end{aligned} \tag{S1}$$

where I indicates electric current, q is the electric charge, L is the inductance on the SRRs and $\omega_0 = \frac{1}{\sqrt{LC}}$ with capacitance C is the resonance frequency. A and l are the effective area and length of SRR, respectively. Substituting Eq.(S1) into the Maxwell equations, a Hermitian Hamiltonian can be obtained to describe the dispersive system

(28),

$$H\psi = N^{-1/2}MN^{-1/2}\psi = E\psi \quad (\text{S2})$$

where,

$$M = \begin{bmatrix} 0 & 0 & 0 & 0 & k_z & -k_y & 0 & 0 & 0 & -i\frac{l}{A} \\ 0 & 0 & 0 & -k_z & 0 & k_x & 0 & 0 & -i\frac{l}{A} & 0 \\ 0 & 0 & 0 & k_y & -k_x & 0 & 0 & 0 & 0 & 0 \\ 0 & -k_z & k_y & 0 & 0 & 0 & 0 & 0 & 0 & 0 \\ k_z & 0 & -k_x & 0 & 0 & 0 & 0 & 0 & 0 & 0 \\ -k_y & k_x & 0 & 0 & 0 & 0 & 0 & 0 & 0 & 0 \\ 0 & 0 & 0 & 0 & 0 & 0 & 0 & 0 & 0 & i\omega_0^2 \frac{L}{lA} \\ 0 & 0 & 0 & 0 & 0 & 0 & 0 & 0 & i\omega_0^2 \frac{L}{lA} & 0 \\ 0 & i\frac{l}{A} & 0 & 0 & 0 & 0 & 0 & -i\omega_0^2 \frac{L}{lA} & 0 & 0 \\ i\frac{l}{A} & 0 & 0 & 0 & 0 & 0 & -i\omega_0^2 \frac{L}{lA} & 0 & 0 & 0 \end{bmatrix} \quad (\text{S3})$$

and N is positive definite,

$$N = \begin{bmatrix} 1 & 0 & 0 & 0 & 0 & 0 & 0 & 0 & 0 & 0 \\ 0 & 1 & 0 & 0 & 0 & 0 & 0 & 0 & 0 & 0 \\ 0 & 0 & 1 & 0 & 0 & 0 & 0 & 0 & 0 & 0 \\ 0 & 0 & 0 & 1 & 0 & 0 & 0 & 0 & 1 & 0 \\ 0 & 0 & 0 & 0 & 1 & 0 & 0 & 0 & 0 & 1 \\ 0 & 0 & 0 & 0 & 0 & 1 & 0 & 0 & 0 & 0 \\ 0 & 0 & 0 & 0 & 0 & 0 & \omega_0^2 \frac{L}{l^2} & 0 & 0 & 0 \\ 0 & 0 & 0 & 0 & 0 & 0 & 0 & \omega_0^2 \frac{L}{l^2} & 0 & 0 \\ 0 & 0 & 0 & 1 & 0 & 0 & 0 & 0 & \frac{L}{A^2} & 0 \\ 0 & 0 & 0 & 0 & 1 & 0 & 0 & 0 & 0 & \frac{L}{A^2} \end{bmatrix} \quad (\text{S4})$$

and,

$$\psi^T = [E_x \ E_y \ E_z \ H_x \ H_y \ H_z \ P_x \ P_y \ M_x \ M_y] \quad (\text{S5})$$

where P and M are electric and magnetic dipole moments, respectively.

In the model, we neglect the ohmic loss and the interactions between intra and inter layers. The corresponding constitutive matrices are,

$$\begin{aligned} \varepsilon &= \begin{bmatrix} 1 + \frac{l^2}{L} \frac{1}{\omega_0^2 - \omega^2} & 0 & 0 \\ 0 & 1 + \frac{l^2}{L} \frac{1}{\omega_0^2 - \omega^2} & 0 \\ 0 & 0 & 1 \end{bmatrix} \\ \mu &= \begin{bmatrix} 1 + \frac{A^2}{L} \frac{\omega^2}{\omega_0^2 - \omega^2} & 0 & 0 \\ 0 & 1 + \frac{A^2}{L} \frac{\omega^2}{\omega_0^2 - \omega^2} & 0 \\ 0 & 0 & 1 \end{bmatrix} \\ \xi &= \begin{bmatrix} 0 & \frac{lA}{L} \frac{\omega}{\omega_0^2 - \omega^2} & 0 \\ \frac{lA}{L} \frac{\omega}{\omega_0^2 - \omega^2} & 0 & 0 \\ 0 & 0 & 0 \end{bmatrix} \end{aligned} \quad (\text{S6})$$

We defined them in Maxwell's equation as,

$$\begin{bmatrix} D \\ B \end{bmatrix} = M \begin{bmatrix} E \\ H \end{bmatrix} = \begin{bmatrix} \varepsilon & i\xi \\ -i\xi & \mu \end{bmatrix} \begin{bmatrix} E \\ H \end{bmatrix} \quad (\text{S7})$$

Here, we have already set $\varepsilon_0 = \mu_0 = c = 1$ for simplicity. From the Maxwell's divergence condition,

$$\begin{cases} \nabla \cdot D = 0 \\ \nabla \cdot B = 0 \end{cases} \quad (\text{S8})$$

One can easily derive that the electromagnetic coupling longitudinal mode (EM-LM) dispersion along ΓM direction is described as,

$$\det \begin{bmatrix} \epsilon_{11} & i\xi_{12} \\ -i\xi_{21} & \mu_{11} \end{bmatrix} = 0. \quad (\text{S9})$$

The electromagnetic field corresponding to this novel longitudinal mode is,

$$\begin{aligned} E_x &= E_y \neq 0 \\ H_x &= H_y \neq 0 \\ E_z &= H_z = 0 \end{aligned} \quad (\text{S10})$$

which is different from normal electric longitudinal mode only having non-zero components in electric field.

Substituting Eq. S6 into Eq. S9, we get the dispersion of EM-LM as,

$$\omega = \frac{\sqrt{l^2 + L\omega_0^2}}{\sqrt{L - A^2}} \quad (\text{S11})$$

which is an exactly flat band without any dispersion.

An example of band dispersion is shown in Fig. S2 with parameters of $l=1, A=0.9, L=1, \omega_0=2$. In crystal, the inter-unit-cell interaction usually bends the longitudinal mode to be dispersive (dashed lines) as schematically shown in Fig. S2. Consequently, the Weyl point (small circle) will subtly shift away from the original location (solid dot). Our design possesses dispersive EM-LM with negative group velocity constructing four type-I Weyl nodes. Interestingly, four symmetry related type-II Weyl nodes can be obtained by adjusting the inter-unit cell interaction.

5. Eigen electric field and symmetry analysis

As mentioned above, the Weyl state space is spanned by two modes, which are transverse mode (TM) and EM-LM. For the TM, most part of the electric field will be perpendicular to $\vec{k}_{\Gamma M}$; while in EM-LM mode, the electric fields majorly orient along $\vec{k}_{\Gamma M}$. After analyzing the eigen electric field simulated in CST, the prediction is confirmed as shown in Fig. S3. The transverse mode can be regarded as right circularly polarized (RCP) with increasing phase, where the electric field rotates clockwise. Overall, most of the energy concentrates on the margin of the primitive unit cell. Comparatively, electric energy density of EM-LM is higher in the center (saddle like metallic structure) region, as shown in Fig. S3C. Magnetic fields (H fields) having similar behaviors are not shown.

The saddle-like structure possesses D_{2d} point group, along ΓM a two-fold rotation is preserved. Here, the TM and EM-LM are belong two different classes of the two-fold rotation symmetry. Thus, the band repulsion between them is forbidden. As shown in Fig. S3B and S3C, they have different eigenvalues,

$$\begin{aligned} R_{\Gamma M}(\pi)E_{TM} &= -E_{TM} \\ R_{\Gamma M}(\pi)E_{EM-LM} &= E_{EM-LM} \end{aligned} \quad (S12)$$

6. Experimental configurations and real space field distribution

Fig. S4 shows two different near field scanning configurations. The corresponding bulk and surface states are shown in an extended Brillouin zone. In setup ‘b’, compared with those surface arc located near BZ boundaries, surface states close to light cone have much higher intensity, they are less bounded and thus easily detected by probe.

7. Chessboard like interference between ideal Weyl nodes

As shown in Fig. S5A to S5C, around the center of the sample, the field distribution forms a periodic square lattice, which slightly increases with the frequency. The plot of the real part of the field in Fig. S5D to S5F shows that the phase of the field exhibits a checkerboard pattern. Their corresponding EFCs (Fig. S5G, H and I), obtained by the Fourier transform of the complex field pattern, show four circles with the same radius increasing with frequency. Apparently, the increase of the lattice constant of the field in the real space with frequency is due to the shift of the bulk EFCs towards the origin of the momentum space at higher frequency. The observation of the robust checkerboard-like interference pattern of the fields further weakly confirms our designed meta-crystal structure is a clean and ideal photonic Weyl system.

8. Dimension reduction process from ideal Weyl points to graphene

Having confirmed the helicoid nature of the surface state arcs, the dispersion of the bulk and surface states along four representative momentum cuts provide further insight into the bulk-surface correspondence hosted by the ideal Weyl meta-crystal. Two of the band dispersions are taken along two straight momentum cuts passing through the Weyl points in the horizontal and vertical direction, by fixing $k_y = 0.4 \pi/a$ (cut I) and $k_x = 0.4 \pi/a$ (cut III), respectively (Fig. S6C). Along the horizontal momentum cut, it is observed that a surface state connects directly between the two Weyl points within the BZ (Fig. S6A, I), which is reminiscent of the bearded edge state connection between the Dirac points in graphene. On the other hand, along the vertical momentum cut, the two Weyl points are connected by a surface state crossing the boundary of BZ (Fig. S6A, III), reminiscent of the edge state connection in graphene along the zigzag termination. For the other two momentum cuts slightly tilted from the horizontal and vertical directions, since they do

not pass through the Weyl points, a complete band gap opens up in each band structure. In each case, it is observed that a single surface state connects between the upper and lower bulk bands across the bandgap, indicating the nontrivial topology of the band structures. The numerically simulated dispersion relation along all the four momentum cuts (Fig. S6B) agree very well with the experimental results (Fig. S6A), further revealing the intriguing bulk surface correspondence present in the Weyl system.

9. Effect of loss

In the microwave regime, the loss of metallic components is usually negligible, as metal (copper here) functions nearly as a perfect electric conductor (PEC), whose penetration depth approaches to zero. The loss in our system mainly arises from the isotropic background dielectric (F4BM220), whose loss is usually characterized by the dielectric loss tangent $\tan\delta = \epsilon''/\epsilon'$, where ϵ'' and ϵ' are the imaginary and real part of the permittivity, respectively. Because the penetration of electromagnetic field into the metal is negligible, all of modes (such as the two modes constructing the Weyl state space) share the same loss induced by the background media. Around 10 GHz its dielectric loss tangent is less than 7×10^{-4} ($\ll 1$), thus the ideal Weyl system has been considered as lossless in the design and measurement.

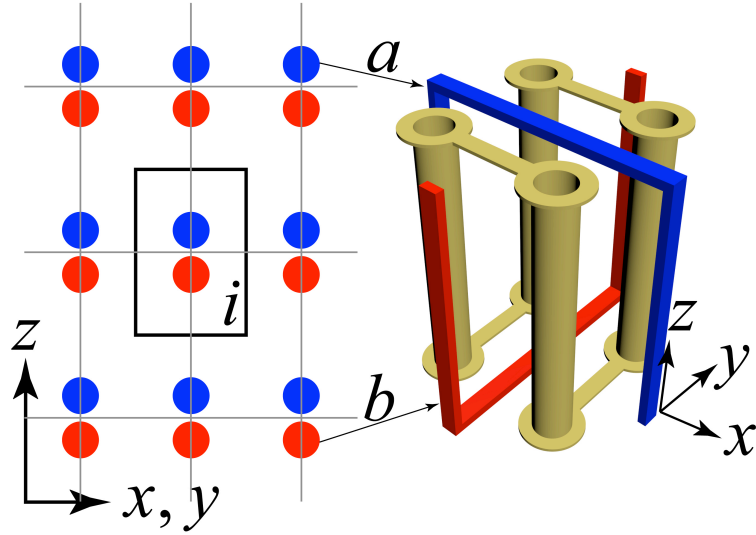


Fig.S1. Effective media model simplification. The period along x , y and z directions are $a_x = a_y = a = 3$ mm and $a_z = 4.5$ mm, respectively, where the unit cell is highlighted by black solid rectangle (projected along x/y direction). Right hand side inset explains how the realistic structure can be effectively simplified to be two splitting resonator rings (SRRs) colored by red and blue. Each SRR can be regarded as an orbital or sub-lattice to describe the low energy excitation around Weyl points.

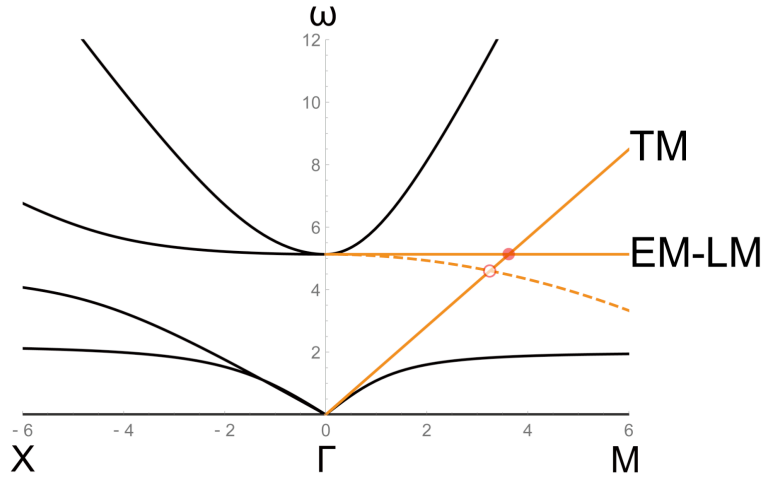


Fig. S2 Band structure along X- Γ -M calculated with effective media model. TM and EM-LM indicate transverse mode and electromagnetic-coupling-longitudinal mode (EM-LM), respectively. Their crossing is Weyl point (solid dot). In realistic structure crystal non-local effect makes the longitudinal mode dispersive with negative group velocity (dashed line) and moves the crossing to a new position, as indicated by the circle.

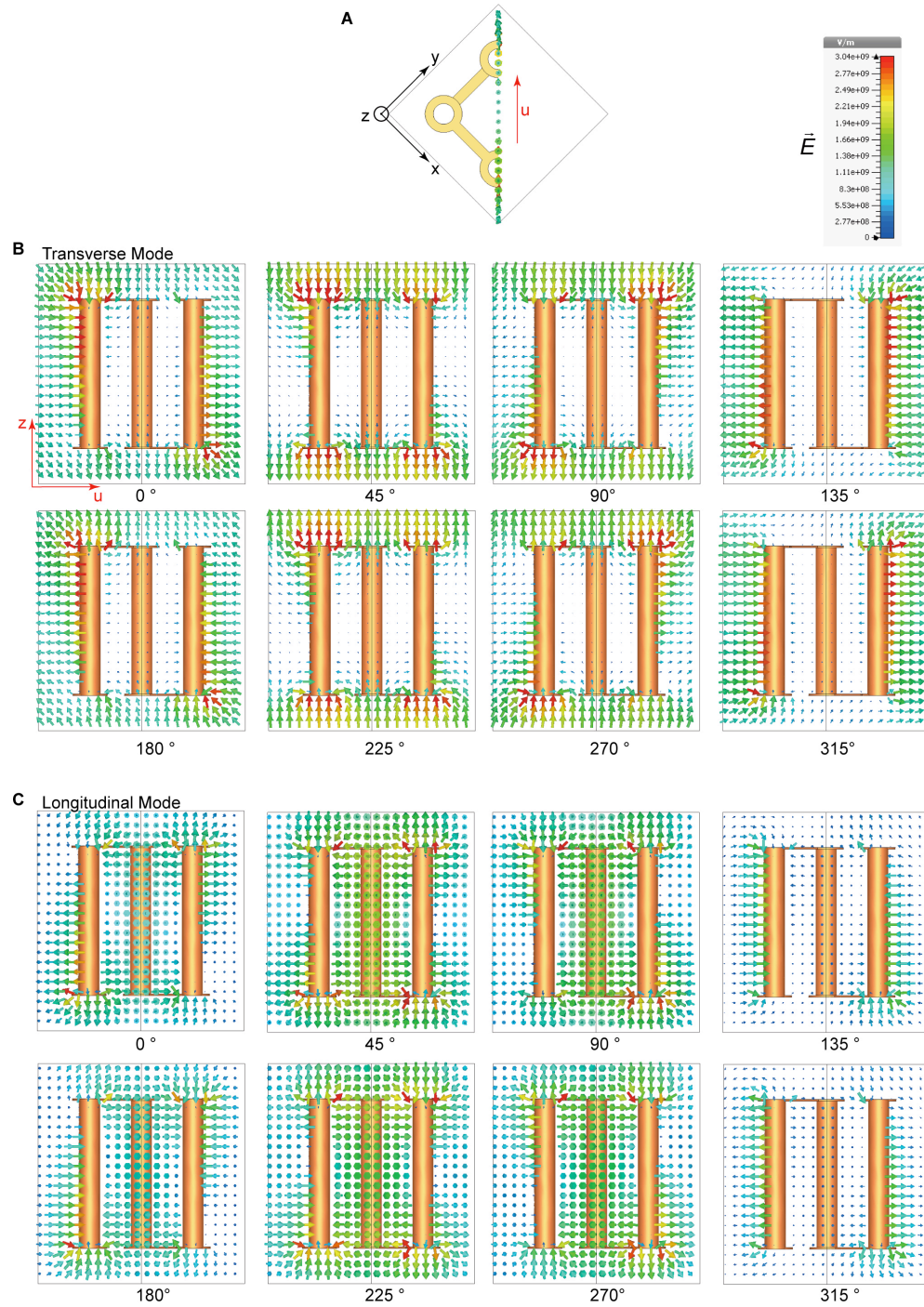


Fig. S3. Eigen electric field profiles for both transverse and longitudinal mode. (A) Cutting plane of the primitive unit cell, on which electric field is exported. **(B)** Eigen-electric field profile of transverse mode with respect of different phases from 0° - 315° in

the step of 45° . (C) Similar to (B) but for the electromagnetic coupling longitudinal mode (EM-LM).

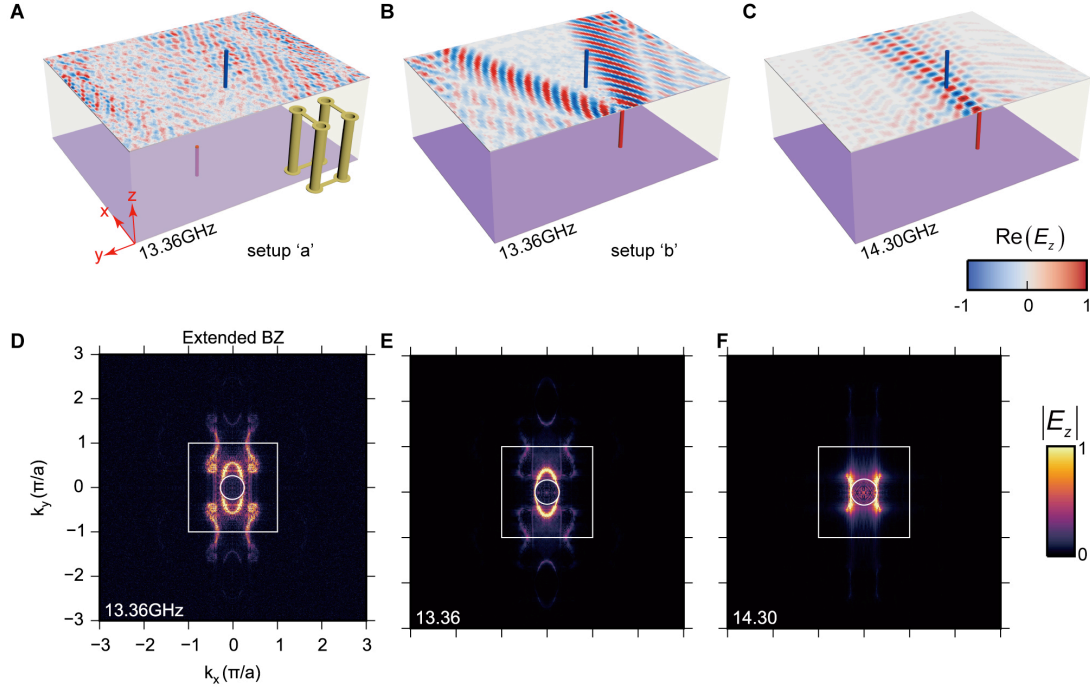


Fig. S4. Configuration of near-field scanning systems. (A), (B) and (C) Different experiment configurations for top surface scanning. The bottom surfaces are highlighted by blue planes. (A) indicates setup ‘a’ where the source is positioned on the bottom surface center, while (B) and (C) represent the setup ‘b’ where the source is located on the top surface edge. The structure orientation is indicated in the inset of (A). Thickness of samples in setup ‘a’ and ‘b’ are $10a_z$ and $20a_z$, respectively. The width and length for both cases are 210 mm and 270 mm, respectively. In (A) and (B), field distributions on top surface are taken from experiment at 13.36 GHz. (C) shows similar field distribution at 14.3 GHz. (D) Equi-frequency contour (EFC) scanned in setup ‘a’ at 13.36 GHz in an extended Brillouin zone. (E) and (F) EFCs scanned in setup ‘b’ with respect of 13.36

GHz and 14.30 GHz, respectively. The first Brillouin zone (BZ) is indicated by the white solid square. The white circle is EFC of light cone at the corresponding frequency.

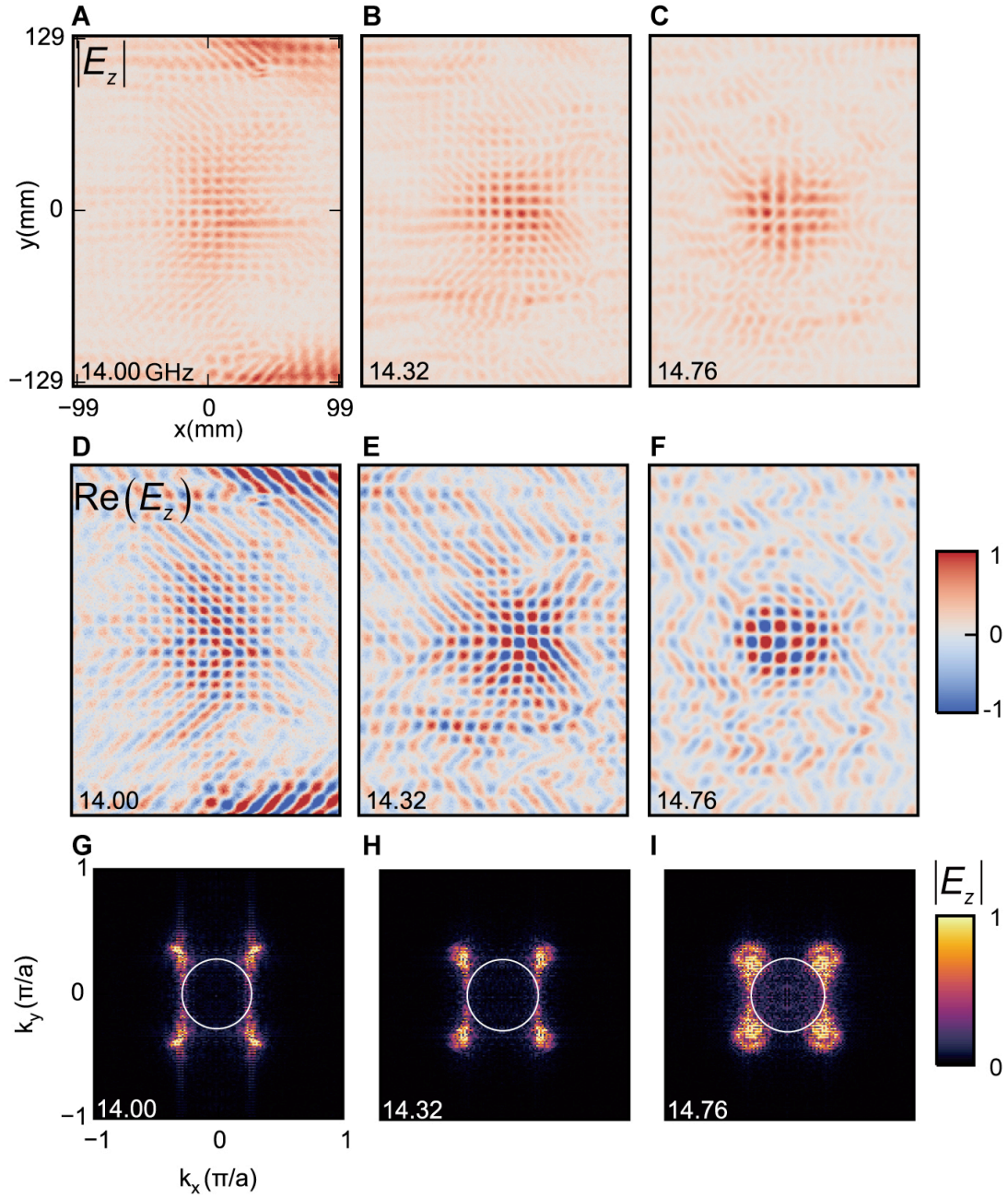


Fig. S5. Chessboard-like interference pattern between four Weyl nodes. (A), (B) and (C) Interference pattern illustrated in amplitude measured with setup ‘a’ at 14.00, 14.32

and 14.76 GHz, respectively. (D)-(F) showing real part of field distributions of (A)-(C). (G)-(I) are the corresponding Fourier transformations. White circle indicates air equi-frequency contour at the corresponding frequency.

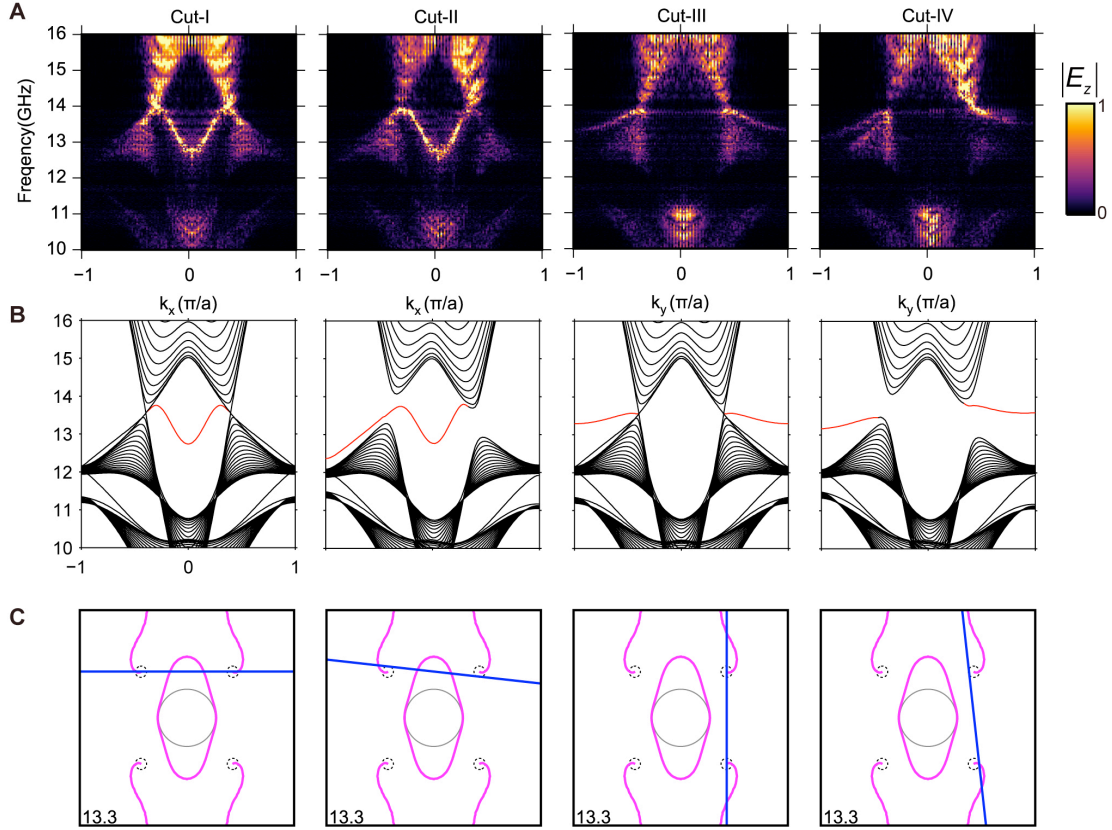


Fig. S6. The measured and simulated dispersions along four different momentum cuts. (A) The measured band structures along the momentum cuts indicated by (C). (B) The simulated band structures where the surface states are drawn in red. Surface states in cut-I and cut-III show strong resemblance to the bearded and zigzag edge states of graphene nanoribbon, respectively. (C) The numerically calculated equi - frequency contour at 13.3 GHz where the momentum cuts (in blue) for the dispersions shown in (A) and (B) are indicated.

References and Notes

1. A. H. Castro Neto, F. Guinea, N. M. R. Peres, K. S. Novoselov, A. K. Geim, The electronic properties of graphene. *Rev. Mod. Phys.* **81**, 109–162 (2009). [doi:10.1103/RevModPhys.81.109](https://doi.org/10.1103/RevModPhys.81.109)
2. X. Wan, A. M. Turner, A. Vishwanath, S. Y. Savrasov, Topological semimetal and Fermi-arc surface states in the electronic structure of pyrochlore iridates. *Phys. Rev. B* **83**, 205101 (2011). [doi:10.1103/PhysRevB.83.205101](https://doi.org/10.1103/PhysRevB.83.205101)
3. A. A. Burkov, L. Balents, Weyl semimetal in a topological insulator multilayer. *Phys. Rev. Lett.* **107**, 127205 (2011). [doi:10.1103/PhysRevLett.107.127205](https://doi.org/10.1103/PhysRevLett.107.127205) [Medline](#)
4. G. Xu, H. Weng, Z. Wang, X. Dai, Z. Fang, Chern semimetal and the quantized anomalous Hall effect in HgCr₂Se₄. *Phys. Rev. Lett.* **107**, 186806 (2011). [doi:10.1103/PhysRevLett.107.186806](https://doi.org/10.1103/PhysRevLett.107.186806) [Medline](#)
5. N. P. Armitage, E. J. Mele, A. Vishwanath, Weyl and Dirac Semimetals in Three Dimensional Solids. arXiv:1705.01111 [cond-mat.str-el], (2017). <https://arxiv.org/abs/1705.01111>
6. S.-Y. Xu, I. Belopolski, N. Alidoust, M. Neupane, G. Bian, C. Zhang, R. Sankar, G. Chang, Z. Yuan, C.-C. Lee, S.-M. Huang, H. Zheng, J. Ma, D. S. Sanchez, B. Wang, A. Bansil, F. Chou, P. P. Shibayev, H. Lin, S. Jia, M. Z. Hasan, TOPOLOGICAL MATTER. Discovery of a Weyl fermion semimetal and topological Fermi arcs. *Science* **349**, 613–617 (2015). [doi:10.1126/science.aaa9297](https://doi.org/10.1126/science.aaa9297) [Medline](#)
7. H. Weng, C. Fang, Z. Fang, B. A. Bernevig, X. Dai, Weyl Semimetal Phase in Noncentrosymmetric Transition-Metal Monophosphides. *Phys. Rev. X* **5**, 011029 (2015). [doi:10.1103/PhysRevX.5.011029](https://doi.org/10.1103/PhysRevX.5.011029)
8. A. A. Soluyanov, D. Gresch, Z. Wang, Q. Wu, M. Troyer, X. Dai, B. A. Bernevig, Type-II Weyl semimetals. *Nature* **527**, 495–498 (2015). [doi:10.1038/nature15768](https://doi.org/10.1038/nature15768) [Medline](#)
9. L. Lu, Z. Wang, D. Ye, L. Ran, L. Fu, J. D. Joannopoulos, M. Soljačić, TOPOLOGICAL MATTER. Experimental observation of Weyl points. *Science* **349**, 622–624 (2015). [doi:10.1126/science.aaa9273](https://doi.org/10.1126/science.aaa9273) [Medline](#)
10. L. Huang, T. M. McCormick, M. Ochi, Z. Zhao, M.-T. Suzuki, R. Arita, Y. Wu, D. Mou, H. Cao, J. Yan, N. Trivedi, A. Kaminski, Spectroscopic evidence for a type II Weyl semimetallic state in MoTe₂. *Nat. Mater.* **15**, 1155–1160 (2016). [doi:10.1038/nmat4685](https://doi.org/10.1038/nmat4685) [Medline](#)
11. W.-J. Chen, M. Xiao, C. T. Chan, Photonic crystals possessing multiple Weyl points and the experimental observation of robust surface states. *Nat. Commun.* **7**, 13038 (2016). [doi:10.1038/ncomms13038](https://doi.org/10.1038/ncomms13038) [Medline](#)
12. J. Noh, S. Huang, D. Leykam, Y. D. Chong, K. P. Chen, M. C. Rechtsman, Experimental observation of optical Weyl points and Fermi arc-like surface states. *Nat. Phys.* **13**, 611–617 (2017). [doi:10.1038/nphys4072](https://doi.org/10.1038/nphys4072)
13. B. Yang, Q. Guo, B. Tremain, L. E. Barr, W. Gao, H. Liu, B. Béri, Y. Xiang, D. Fan, A. P. Hibbins, S. Zhang, Direct observation of topological surface-state arcs in photonic metamaterials. *Nat. Commun.* **8**, 97 (2017). [doi:10.1038/s41467-017-00134-1](https://doi.org/10.1038/s41467-017-00134-1) [Medline](#)

14. C. Fang, L. Lu, J. Liu, L. Fu, Topological semimetals with helicoid surface states. *Nat. Phys.* **12**, 936–941 (2016). [doi:10.1038/nphys3782](https://doi.org/10.1038/nphys3782)
15. J. Ruan, S.-K. Jian, H. Yao, H. Zhang, S.-C. Zhang, D. Xing, Symmetry-protected ideal Weyl semimetal in HgTe-class materials. *Nat. Commun.* **7**, 11136 (2016). [doi:10.1038/ncomms11136](https://doi.org/10.1038/ncomms11136) [Medline](#)
16. J. Ruan, S.-K. Jian, D. Zhang, H. Yao, H. Zhang, S.-C. Zhang, D. Xing, Ideal Weyl Semimetals in the Chalcopyrites CuTlSe₂, AgTlTe₂, AuTlTe₂, and ZnPbAs₂. *Phys. Rev. Lett.* **116**, 226801 (2016). [doi:10.1103/PhysRevLett.116.226801](https://doi.org/10.1103/PhysRevLett.116.226801) [Medline](#)
17. L. Wang, S.-K. Jian, H. Yao, Topological photonic crystal with equifrequency Weyl points. *Phys. Rev. A* **93**, 061801 (2016). [doi:10.1103/PhysRevA.93.061801](https://doi.org/10.1103/PhysRevA.93.061801)
18. T. Kaelberer, V. A. Fedotov, N. Papasimakis, D. P. Tsai, N. I. Zheludev, Toroidal dipolar response in a metamaterial. *Science* **330**, 1510–1512 (2010). [doi:10.1126/science.1197172](https://doi.org/10.1126/science.1197172) [Medline](#)
19. Materials and methods are available as supplementary materials.
20. Q. Guo, W. Gao, J. Chen, Y. Liu, S. Zhang, Line Degeneracy and Strong Spin-Orbit Coupling of Light with Bulk Bianisotropic Metamaterials. *Phys. Rev. Lett.* **115**, 067402 (2015). [doi:10.1103/PhysRevLett.115.067402](https://doi.org/10.1103/PhysRevLett.115.067402) [Medline](#)
21. M. Xiao, Q. Lin, S. Fan, Hyperbolic Weyl Point in Reciprocal Chiral Metamaterials. *Phys. Rev. Lett.* **117**, 057401 (2016). [doi:10.1103/PhysRevLett.117.057401](https://doi.org/10.1103/PhysRevLett.117.057401) [Medline](#)
22. T. Zhang *et al.*, Double-Weyl phonons in transition-metal monosilicides. arXiv:1705.07244 [cond-mat.mtrl-sci], (2017). <https://arxiv.org/abs/1705.07244>
23. Q. Ma, S.-Y. Xu, C.-K. Chan, C.-L. Zhang, G. Chang, Y. Lin, W. Xie, T. Palacios, H. Lin, S. Jia, P. A. Lee, P. Jarillo-Herrero, N. Gedik, Direct optical detection of Weyl fermion chirality in a topological semimetal. *Nat. Phys.* **13**, 842–847 (2017). [doi:10.1038/nphys4146](https://doi.org/10.1038/nphys4146)
24. M. Onoda, S. Murakami, N. Nagaosa, Hall effect of light. *Phys. Rev. Lett.* **93**, 083901 (2004). [doi:10.1103/PhysRevLett.93.083901](https://doi.org/10.1103/PhysRevLett.93.083901) [Medline](#)
25. M. Zhou, L. Ying, L. Lu, L. Shi, J. Zi, Z. Yu, Electromagnetic scattering laws in Weyl systems. *Nat. Commun.* **8**, 1388 (2017). [doi:10.1038/s41467-017-01533-0](https://doi.org/10.1038/s41467-017-01533-0) [Medline](#)
26. R. Zhao, T. Koschny, C. M. Soukoulis, Chiral metamaterials: Retrieval of the effective parameters with and without substrate. *Opt. Express* **18**, 14553–14567 (2010). [doi:10.1364/OE.18.014553](https://doi.org/10.1364/OE.18.014553) [Medline](#)
27. A. Raman, S. Fan, Photonic band structure of dispersive metamaterials formulated as a Hermitian eigenvalue problem. *Phys. Rev. Lett.* **104**, 087401 (2010). [doi:10.1103/PhysRevLett.104.087401](https://doi.org/10.1103/PhysRevLett.104.087401) [Medline](#)